ADVANCED THERAPEUTICS
www.advtherap.com

Combining Photothermal Therapy-Induced Immunogenic Cell Death and Hypoxia Relief-Benefited M1-Phenotype Macrophage Polarization for Cancer Immunotherapy

*Min Zhou, Xiaoyu Wang, Shichao Lin, Yufeng Liu, Junshu Lin, Bo Jiang, Xiaozhi Zhao, and Hui Wei**

The promise of anti-tumor immunotherapy is limited partially by low antigen exposure and the hypoxic tumor microenvironment. To address these two limitations simultaneously, herein, a multifunctional AuNR@BSA/MnO_2 to enable photothermal therapy-induced immunogenic cell death (ICD) and hypoxia relief-benefited M1 polarization of macrophages for enhanced cancer immunotherapy, is designed. The ICD and M1 polarization are demonstrated both in vitro and in vivo by detecting the corresponding markers. Then, enhanced immunotherapeutic efficacy is achieved in a 4T1 tumor-bearing mice model. Additionally, when combined with a checkpoint blockade therapy (PD-1 inhibitor), the AuNR@BSA/MnO_2 shows distant effects including anti-distant tumor, anti-metastasis, and even improved survival. Last, the AuNR@BSA/MnO_2 has multi-imaging functions, such as photoacoustic imaging and magnetic resonance imaging. This study provides a new strategy to design multifunctional nanomedicines for improving anti-tumor immunotherapy and imaging guided therapy.

1. Introduction

Cancer immunotherapy as an advanced treatment has been studied for years, including immune checkpoint blockade (e.g., PD-1/PD-L1 and CTLA-4), chimeric antigen receptor (CAR)-T cell therapy and so on.[1–3] However, these immunotherapies still face the challenge of low response in certain patients.[4–6] One reason for the low response is the limited cytotoxic T lymphocytes infiltration which is caused by no effective antigens exposure and high interstitial pressure of solid tumors.[7] Another reason is the recruitment of the immunosuppressive cells (MDSCs: myeloid-derived suppressor cells, Tregs: regulatory T cells, and TAMs: tumor-associated macrophages), which could be attributed to the tumor microenvironments such as low pH value and low oxygen content.[8,9] Therefore, we reason that increasing antigen exposure and modulating the tumor microenvironment simultaneously would improve the cancer immunotherapy.

Among various strategies developed to increase antigen exposure, phototherapy including photothermal therapy (PTT) and photodynamic therapy (PDT) is very promising because it is clinically used with high spatial and temporal control as well as minimal invasiveness. PTT converts light into heat and ablates tumors while PDT produces highly active singlet oxygen from oxygen by illuminating a photosensitizer. Compared with PDT, PTT has several advantages including deeper penetration due to the near infrared (NIR) absorbance of photothermal agents, broader scope of photothermal agents (such as organic dyes and nanomaterials), and oxygen independence.[10–12] Generally PTT causes cell death via two mechanisms: necrosis and apoptosis. Necrosis would release the antigens which could initiate the innate/adaptive immunity, known as damage-associated molecular patterns (DAMPs); meanwhile apoptosis could generate "find me" and "eat me" signals for recruitment and recognition of dendritic cells (DCs), and could also cause secondary necrosis.[3,13–15] Recently, a few studies revealed that PTT could induce the immunogenic cell death (ICD) and subsequently release DAMP molecules to improve anti-tumor immunogenicity.[16–18]

Meanwhile modulating tumor microenvironment has also attracted much interest, especially improving tumor hypoxia.

M. Zhou, X. Wang, S. Lin, Y. Liu, J. Lin, H. Wei
Department of Biomedical Engineering, College of Engineering and Applied Sciences, Nanjing National Laboratory of Microstructures, Jiangsu Key Laboratory of Artificial Functional Materials
Nanjing University
Nanjing 210023, China
E-mail: weihui@nju.edu.cn; huiwei.hw@gmail.com

B. Jiang, X. Zhao
Department of Urology, Drum Tower Hospital, Medical School of Nanjing University
Institute of Urology
Nanjing University
Nanjing 210008, China

J. Lin
Department of Biomaterials, College of Materials
Xiamen University
Xiamen 361005, China

H. Wei
State Key Laboratory of Analytical Chemistry for Life Science and State Key Laboratory of Coordination Chemistry, School of Chemistry and Chemical Engineering, Chemistry and Biomedicine Innovation Center (ChemBIC)
Nanjing University
Nanjing 210023, China

DOI: 10.1002/adtp.202000191

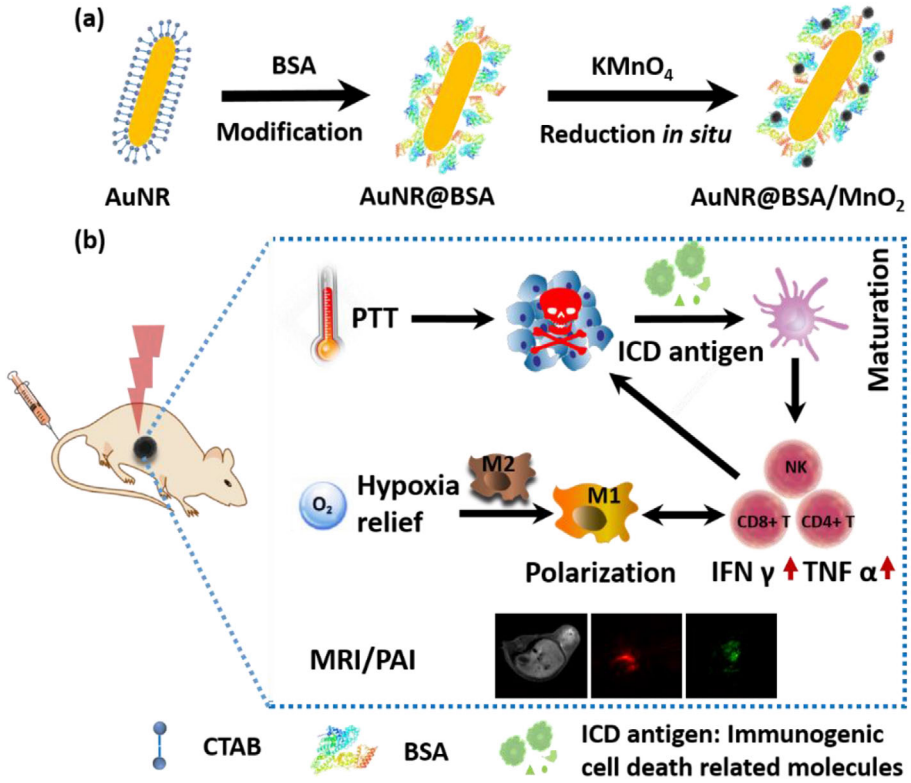

Scheme 1. Photothermal therapy (PTT)-mediated ICD and hypoxia relief-benefited M1 polarization for combined cancer therapy. a) Synthetic processes of AuNR@BSA/MnO_2. b) Scheme of PTT-mediated ICD and hypoxia relief-benefited M1 polarization of macrophages as well as imaging functions of AuNR@BSA/MnO_2.

Generally, several hypoxia-induced chemokines like HIF 1α (hypoxia-induced factor 1α) are expressed due to the hypoxic tumor microenvironment, and the hypoxia-induced chemokines then attract more TAMs infiltration. The initial infiltrating TAMs are M1. But after long-time exposure in hypoxia microenvironment, these M1 TAMs are polarized into pro-tumoral M2 TAMs. Furthermore, the degree of hypoxia is aggravated because of the rapid proliferation of tumor cells, so the hypoxia has been regarded as one of the main reasons for the M2 TAMs' polarization. Tumor hypoxia can be improved by delivering oxygen externally or by generating oxygen endogenously. We and others have demonstrated that manganese oxide nanoparticles generated oxygen from hydrogen peroxide (H_2O_2) in situ and subsequently facilitated the anti-tumoral M1 type TAMs polarization.[19–22] Nevertheless, the combination of PTT-induced ICD and hypoxia improvement-mediated M1 polarization has rarely been explored.

In this study, we designed a multifunctional AuNR@BSA/MnO_2 (AuNR, gold nanorod; BSA, bovine serum albumin) to enable PTT-induced ICD and hypoxia improvement simultaneously for cancer immunotherapy (**Scheme 1**). We chose AuNR as a PTT photoagent due to its strong localized surface plasmon resonance (LSPR) and high photothermal conversion efficiency,[23] and MnO_2 NPs as an oxygen provider due to its capability of decomposing H_2O_2 into oxygen.[20,24,25] The AuNR and MnO_2 were assembled together by BSA which not only enhanced the biocompatibility of AuNR (AuNR@BSA)[26] but also reduced $KMnO_4$ in situ to produce MnO_2 (AuNR@BSA/MnO_2) (Scheme 1a). Through assessing the released DAMPs after the AuNR-mediated PTT both in vitro and in vivo, we demonstrated that AuNR-mediated PTT could induce ICD and then promote the innate/adaptive immunity by enhancing the $CD4^+/CD8^+$ T cell infiltration in tumor area. Moreover, MnO_2-mediated hypoxia relief benefited the anti-tumoral M1 TAMs polarization and exhibited more effective anti-tumor efficacy. Additionally, by synergizing with the checkpoint therapy (PD-1 inhibitor), the whole system exerted notable distant effects including anti-distant tumor, anti-metastasis, and even the prolonged survival rate. Furthermore, the AuNR@BSA/MnO_2 had multi-imaging functions such as MRI (magnetic resonance imaging) and PAI (photoacoustic imaging). Overall, the designed AuNR@BSA/MnO_2 shows a promising application in enhancing anti-tumor immunotherapy.

2. Results and Discussion

2.1. Synthesis and Characterization of AuNR@BSA/MnO_2

First, AuNR with a longitudinal absorption peak at 808 nm was synthesized as the previous reports.[23,27] Then the AuNR was modified with BSA. Finally, AuNR@BSA/MnO_2 was prepared by reducing $KMnO_4$ in situ (Scheme 1a). The morphology of synthesized AuNRs was characterized by transmission electron microscopy (TEM) imaging as **Figure 1**a, its aspect ratio of length to width was 3.6 (length: 83 ± 10 nm; width: 23 ± 2 nm). To improve the biocompatibility of AuNR, BSA modification was

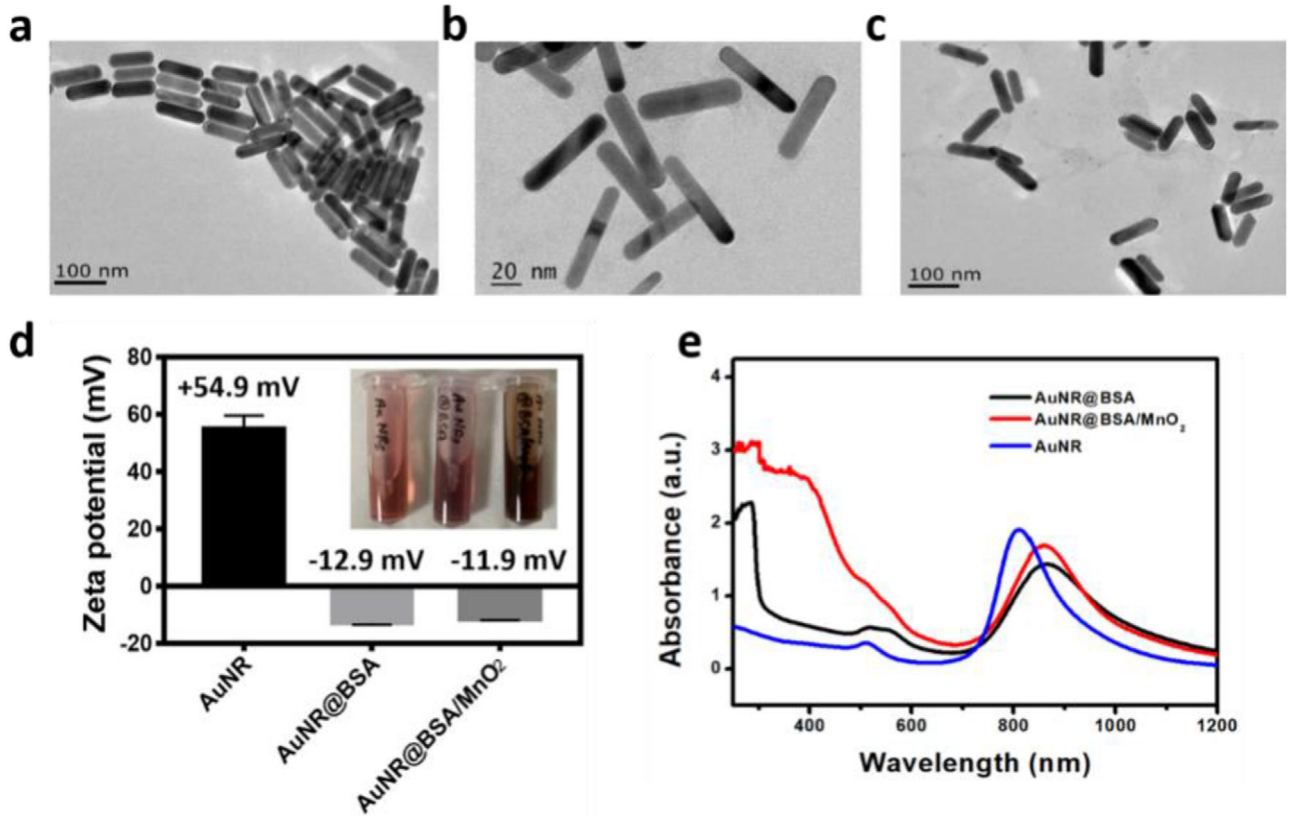

Figure 1. Characterization of gold nanorods (AuNRs). TEM images of a) AuNR, b) AuNR@BSA , and c) AuNR@BSA/MnO_2. d) Zeta potentials of AuNR, AuNR@BSA, and AuNR@BSA/MnO_2. Inset: digital photo of AuNR, AuNR@BSA, and AuNR@BSA/MnO_2. e) UV–vis–NIR spectra of AuNR, AuNR@BSA, and AuNR@BSA/MnO_2.

executed according to a previous report.[28] Highly dispersed BSA-modified AuNR (AuNR@BSA) was observed in Figure 1b and the successful BSA-modification was also confirmed by sodium dodecyl sulfate-polyacrylamide (SDS-PAGE) gel electrophoresis in Figure S1, Supporting Information. With the help of BSA, MnO_2 was produced by reduction of $KMnO_4$ in situ. Figure 1c shows a typical TEM image of AuNR@BSA/MnO_2 NPs. The formation of MnO_2 was confirmed by characteristic lattice stripes in Figure S2b, Supporting Information. The Mn content of AuNR@BSA/MnO_2 was about 6.8 wt%, as measured by using ICP-OES (inductively coupled plasma optical emission spectroscopy). Figure 1d shows the zeta-potentials of synthesized AuNRs. The pristine AuNR was positively charged because of the capped CTAB. After the BSA modification, both AuNR@BSA and AuNR@BSA/MnO_2 were negatively charged. Ultraviolet–visible–NIR (UV–vis–NIR) absorption spectra of AuNRs were recorded in Figure 1e. The pristine AuNR showed a longitudinal absorption peak at 808 nm, while the longitudinal absorption peaks of AuNR@BSA and AuNR@BSA/MnO_2 showed a slight red shift. This may be due to the modification of BSA. A 280 nm peak from BSA was observed for both AuNR@BSA and AuNR@BSA/MnO_2, further indicating the successful coating of BSA. The gradual color change of AuNRs shown in the inset digital photo of Figure 1e was another indicator of successive modification of BSA and growth of MnO_2. Meanwhile the synthesized AuNR@BSA/MnO_2 exhibited good stability in both water and culture medium after incubation for 24 h (Figure S3, Supporting Information).

2.2. Photothermal Effect, Oxygenation, and MRI Abilities

The AuNRs exhibited an absorbance in NIR area as in Figure 1e, so we explored their photothermal effect. When the AuNRs were irradiated under a laser of 808 nm at 0.5 W cm^{-2} at a concentration of 20 μg mL^{-1} (Au concentration), the temperature increased with the increase of laser irradiation time in **Figure 2**a. The temperature of AuNR reached as high as 56 °C while the PBS group showed minimal increase (Figure 2b). The temperatures of AuNR@BSA and AuNR@BSA/MnO_2 increased significantly under laser irradiation, which clearly indicated that BSA coating had no obvious influence on the photothermal effect of AuNR. And AuNR@BSA/MnO_2 showed good photostability under the cycles of laser irradiation (Figure S4, Supporting Information).

Additionally, AuNR@BSA/MnO_2 could decompose H_2O_2 into O_2 by MnO_2.[22,29] To detect the oxygenation, dissolved oxygen content was measured with an oxygen electrode by incubating 5 mM H_2O_2 and 20 μg mL^{-1} AuNR@BSA/MnO_2 (Au concentration, Mn concentration was about 1.36 μg mL^{-1}) together. As shown in Figure 2c, AuNR@BSA/MnO_2 produced the largest amount of dissolved oxygen when compared with the other two

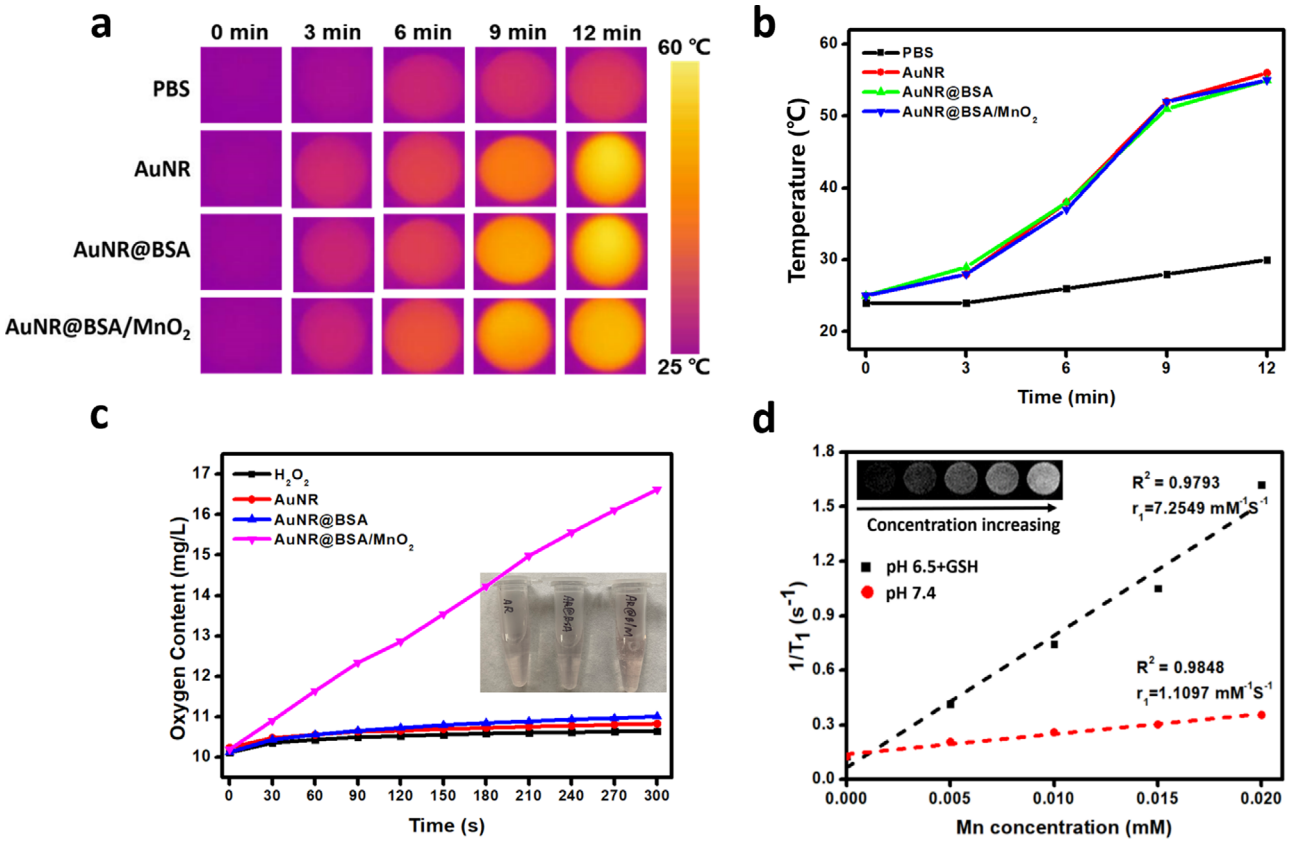

Figure 2. Photothermal effect, oxygenation, and MRI abilities of synthesized AuNRs. a) Thermal imaging of different AuNRs according to the time changing (808 nm laser, 0.5 W cm^{-2}). b) Quantification of temperature change of AuNRs according to thermal imaging in panel (a). c) Kinetic curves of oxygen generation from the decomposition of H_2O_2 in the presence of AuNRs (Mn concentration was about 1.36 μg mL^{-1}). d) T_1-MRI ability of AuNR@BSA/MnO_2 under different conditions.

AuNRs, which could be attributed to H_2O_2 decomposing ability of MnO_2.

Accompanying with H_2O_2 decomposition, Mn^{2+} was released which could be used for T_1 MRI imaging. Next we investigated the MRI ability of AuNR@BSA/MnO_2 by incubating it in two types of buffers as pH 6.5 + 2 mM GSH and pH 7.4. The two buffers imitated the cancerous and normal microenvironments, respectively. Figure 2d clearly revealed that brightness of MRI was concentration dependent. The r_1 in pH 6.5 + 2 mM GSH buffer was 7.25 mM^{-1} s^{-1} while r_1 in pH 7.4 buffer was only 1.11 mM^{-1} s^{-1}. This difference was due to the higher Mn^{2+} releasing under pH 6.5 + 2 mM GSH condition. Consequently, AuNR@BSA/MnO_2 could be used for tumor microenvironment responsive MRI due to the higher GSH content and mild acidic tumor microenvironment.

2.3. PTT-Mediated ICD In Vitro

With the above properties of synthesized AuNRs, we explored their cytotoxicity in Figure S5, Supporting Information. Pristine AuNR without BSA modification showed the highest cytotoxicity to 4T1 cells even in low concentration in Figure S5a, Supporting Information, while AuNR@BSA demonstrated good biocompatibility to cells even in high concentration in Figure S5b, Supporting Information. AuNR@BSA/MnO_2 exhibited a dose-dependent toxicity to cells due to the presence of MnO_2. 10 μg mL^{-1} was an acceptable concentration with minimal toxicity and was chosen for later cellular studies. In Figure S5d, Supporting Information, we clearly observed that with the 808 nm laser irradiation, cell viability decreased in a dose-depended manner. TEM images of AuNR@BSA/MnO_2 both in RAW264.7 and 4T1 cells were obtained (Figure S6, Supporting Information). AuNR@BSA/MnO_2 in lysosomes and other organelles were observed, indicating a possible endocytosis mediated by lysosomes. Based on cytotoxicity and cell uptaking analysis, next we investigated whether the AuNR mediated-PTT would facilitate the ICD and release the antigens. These antigens as the major components of ICD include high mobility group protein box 1 (HMGB1), adenosine triphosphate (ATP), and calreticulin (CRT). These signals can promote the maturation of dendritic cells (DCs), and subsequently initiate the adaptive immunity.[30,31]

HMGB1 is located in the nucleus of cells. Tumor cells would secrete HMGB1 into extracellular environment upon some treatments like PDT or chemotherapy. These released HMGB1 would promote the phagocytosis of immune cells and initiate the immune system.[32] Here we observed the HMGB1 release by confocal laser scanning microscope (CLSM). As shown in **Figure 3**a, under the laser irradiation, the content of HMGB1 decreased in AuNR@BSA and AuNR@BSA/MnO_2 groups while no laser

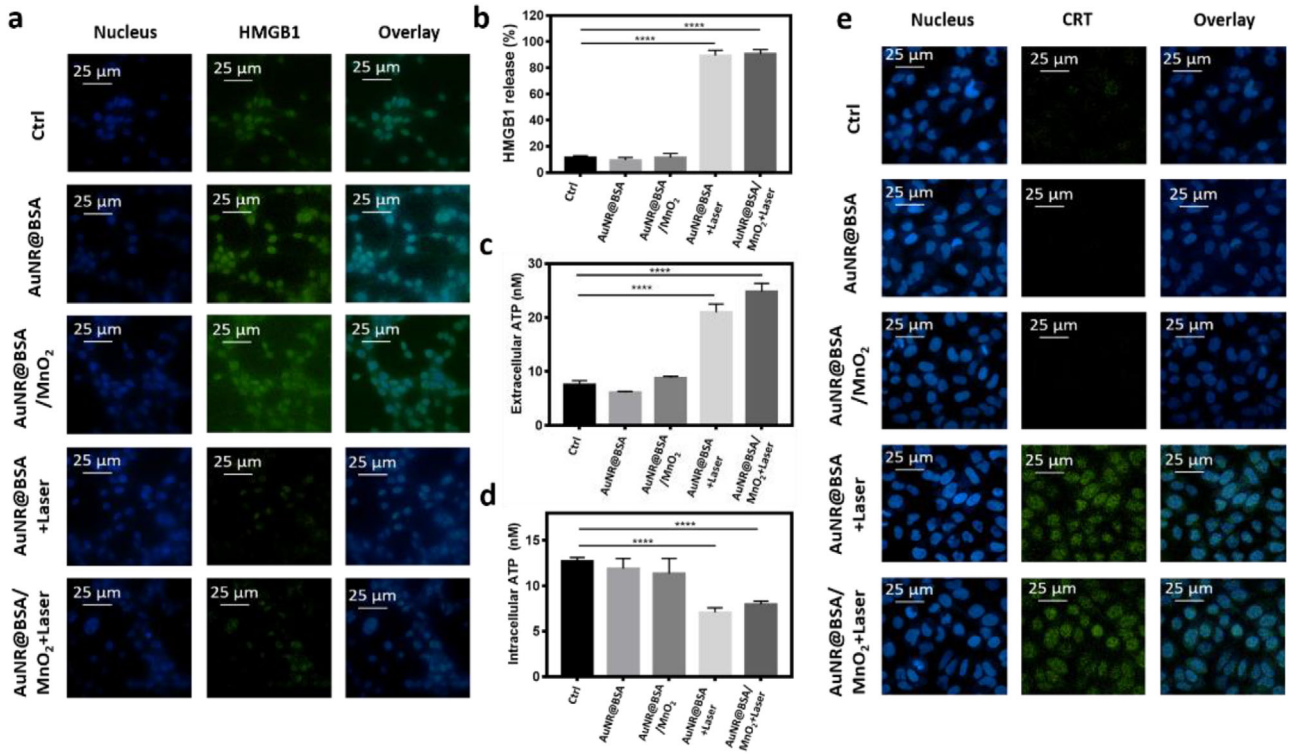

Figure 3. PTT-mediated ICD in vitro. a) Detection of HMGB1 secretion under different treatments by CLSM. b) Quantification of the secretion of HMGB1 under different treatments by measuring the fluorescence intensity. c,d) Quantification of the levels of extracellular and intracellular ATP content under different treatments. e) CLSM analysis of CRT expression. Here concentration of AuNRs was 10 μg mL^{-1} and laser treatment was 1 W cm^{-2} for 5 min. Error bars indicate standard deviations of four independent detections. Data was analyzed by ordinary one-way ANOVA, ****$p < 0.0001$.

groups showed a higher content of HMGB1 in cells. The released HMGB1 was also quantified by fluorescence intensity in Figure 3b. As high as 89.3% and 90.0% HMGB1 was released in AuNR@BSA and AuNR@BSA/MnO_2 groups with laser irradiation, respectively.

ATP release was another hallmark of ICD. The released ATP would facilitate the recruitment of DCs.[33] We evaluated both the intracellular and extracellular levels of ATP in Figure 3c,d and Figure S3a,b, Supporting Information. Extracellular ATP contents at 4 h after laser irradiation were up to 3.0-fold and 3.4-fold, respectively in AuNR@BSA and AuNR@BSA/MnO_2 groups when compared with control group (Figure 3c). While the intracellular ATP contents in AuNR@BSA and AuNR@BSA/MnO_2 groups were less than control group at 4 h after laser irradiation (Figure 3d). The different levels of ATP were contributed to PTT-mediated ATP releasing. Meanwhile we also measured both intracellular and extracellular levels of ATP at 12 h after laser irradiation; very similar results were demonstrated in Figure S7, Supporting Information. Increase of extracellular ATP and decrease of intracellular ATP were another evidence for ICD.

CRT, which belongs to the heat shock protein family, has been regarded as one of the tumor immunogenic mediators.[34,35] By using CLSM, we discovered that the exposure of CRT increased with the laser irradiation in Figure 3e. Altogether, based on the release of HMGB1 and ATP and the increased exposure of CRT after the photothermal effect, we concluded that AuNRs-mediated PTT could elicit the ICD. Next, we performed anti-tumor studies in vivo to investigate the therapeutic efficacy of AuNRs.

2.4. PTT-Mediated ICD In Vivo

Now that photothermal effect induced the ICD in vitro, we sought to explore its anti-tumor ability. We chose a 4T1 tumor-bearing mice model. AuNR@BSA and AuNR@BSA/MnO_2 were intravenously administered. First, we measured the photothermal effect of different treatments in **Figure 4**a,b. Under the 808 nm laser irradiation, the temperature increased along with the time increasing (Figure 4a). The highest temperatures in AuNR@BSA and AuNR@BSA/MnO2 were 52.3 and 52.7 °C, respectively (Figure 4b). Tumors were ablated in both AuNR@BSA and AuNR@BSA/MnO_2 with laser irradiation, down to 2/3 and 1/3 of the original volume, respectively (Figure 4c). To verify the PTT-induced ICD in vivo, we performed the immune fluorescent analysis of dissected tumors. CRT and HMGB1 as two hallmarks were detected in Figure 4d–g. It showed that the expression of CRT was high with the laser irradiation while the expression was low without the laser irradiation (Figure 4d,e). This result indicated that PTT could induce the CRT expression in vivo. HMGB1 as a nucleus-binding protein is over-expressed in tumors. Its content in nuclear area was down to 33% and 30% in AuNR@BSA and AuNR@BSA/MnO_2 with laser groups,

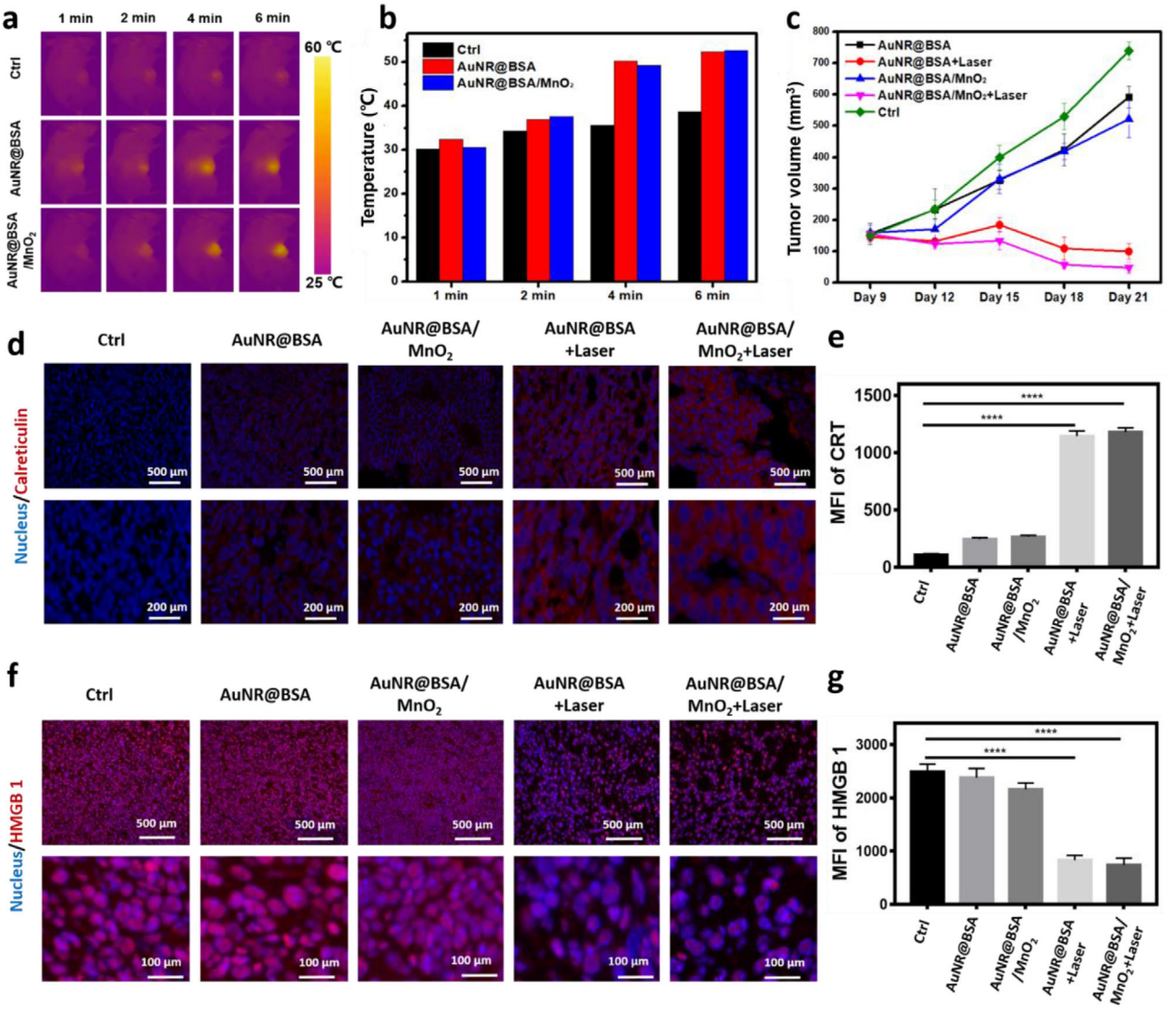

Figure 4. PTT-mediated ICD in vivo. a) Photothermal imaging of tumor area after intravenous injection of indicated materials and laser irradiation. b) Quantification of temperature increase with the expanding time. c) Tumor volume changes under different treatments. d) CRT expression under different treatments by CLSM. Upper is under low magnification and lower is under high magnification. e) Mean fluorescence intensity (MFI) of CRT. f) HMGB1 distribution under different treatments by CLSM. Upper is under low magnification and lower is under high magnification. g) MFI of HMGB1 in nuclear areas. AuNRs treating concentration was 5 mg kg^{-1} and laser intensity was 2 W cm^{-2} for 5 min. Error bars indicate standard deviations of four independent detections. Data was analyzed by ordinary one-way ANOVA, ****$p < 0.0001$.

respectively (Figure 4f,g). Increase of CRT expression and decrease of HMGB1 were consistent with the cellular studies. These results further demonstrated that AuNRs-mediated PTT facilitated the ICD in vivo.

2.5. Anti-Tumor Mechanism

Since the AuNRs-mediated PTT promoted the ICD both in vitro and in vivo, we attempted to investigate the anti-tumor mechanism. Here we detected two types of cytokines in whole blood of mice, including IFN γ and TNF α (**Figure 5**a,b). For both the cytokines, AuNR@BSA/MnO_2 with laser irradiation exhibited the highest content and AuNR@BSA with laser irradiation showed a higher content than others without laser irradiation. These results were consistent with anti-tumor ability of AuNRs. To further verify PTT-mediated ICD would benefit the immunity, we evaluated the T cells' infiltration in dissected tumors in Figure 5c. Both $CD4^+$ and $CD8^+$ T cells' infiltration was obviously increased in AuNRs with laser. This was not only consistent with the anti-tumor ability but also an indication of activation/promotion of immunity.

Notably, we noticed that AuNRs containing MnO_2 groups (i.e., AuNR@BSA/MnO_2 and AuNR@BSA/MnO_2 + Laser) exhibited higher anti-tumor efficiency than the ones without MnO_2 (i.e., AuNR@BSA and AuNR@BSA + Laser). Previous studies have shown that hypoxia improvement would benefit the immunotherapy.[19–21,36] The ability of AuNR@BSA/MnO_2 of

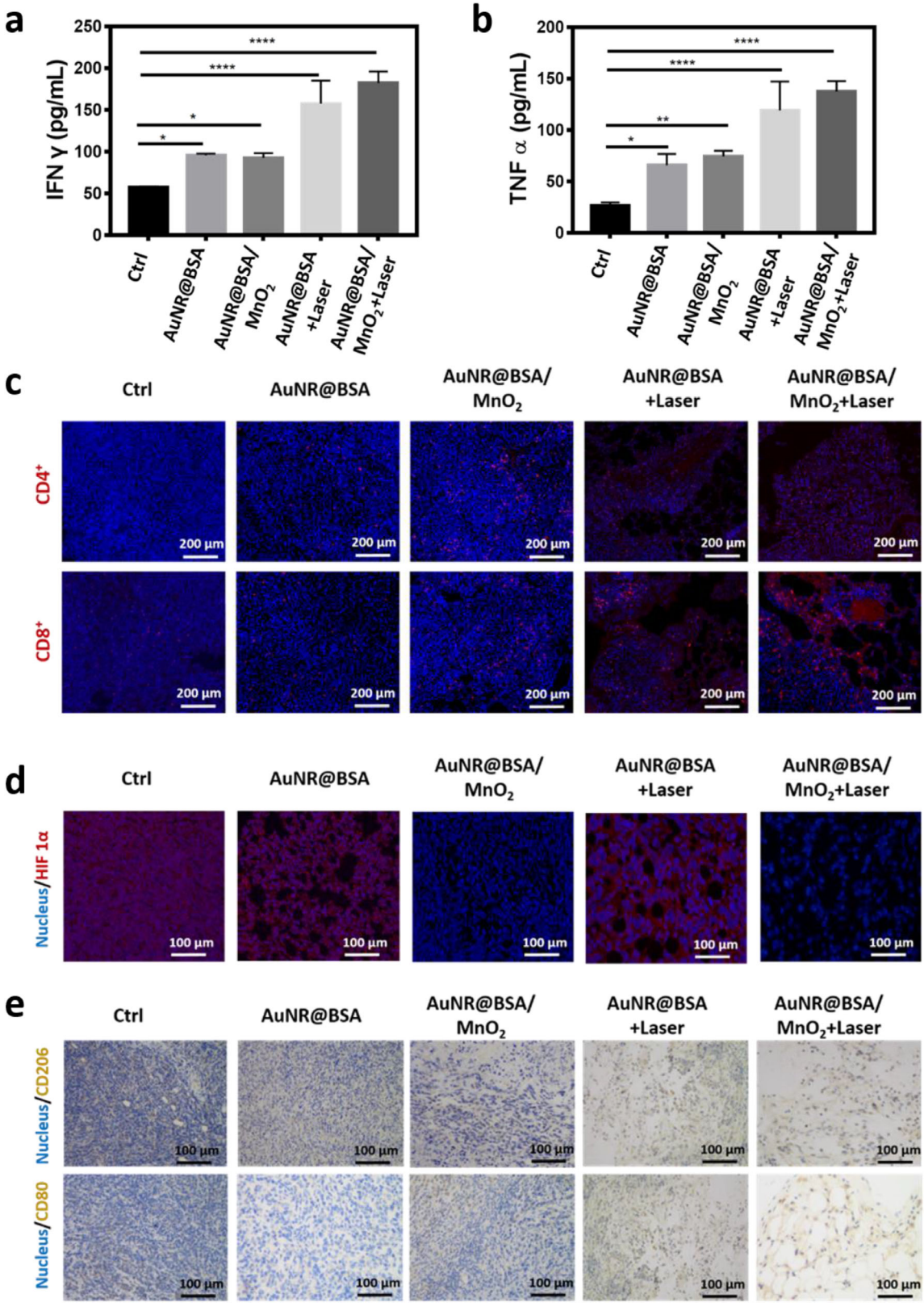

Figure 5. Cytokine detection and anti-tumor mechanism analysis. a,b) Levels of IFN γ and TNF α under different treatments. c) Immunofluorescent analysis of T cells' infiltration in dissected tumors. d) HIF 1α expression in dissected tumors. e) Immunochemical analysis of CD206 and CD80 in dissected tumors. Concentration of AuNRs was 5 mg kg^{-1} and laser intensity was 2 W cm^{-2} for 5 min. Error bars indicated standard deviations of four independent detections. Data was analyzed by ordinary one-way ANOVA, ****$p < 0.0001$.

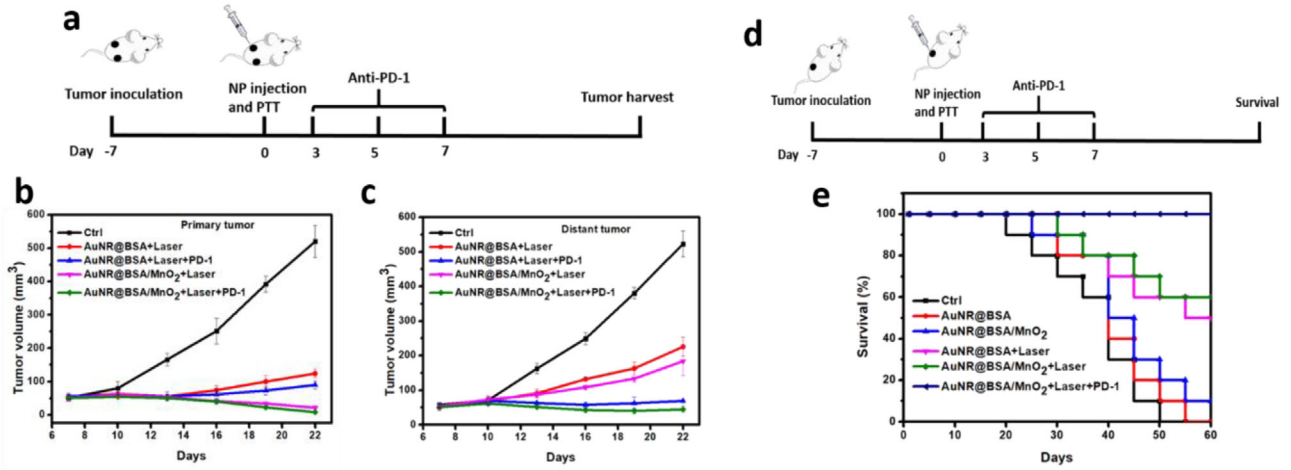

Figure 6. Synergistic effect with checkpoint blockade therapy. a) Scheme of bilateral tumor model. b,c) Primary and distant tumor volume changes under different treatments. d) Scheme of survival model. e) Survival curve of mice by indicated treatments. Error bars indicate standard deviations of four independent detections.

decomposing H_2O_2 into oxygen has been proved in Figure 2c. We further studied this ability at cellular level in Figure S8a,b, Supporting Information. MnO_2 could obviously improve the hypoxia in cells. HIF 1α is an indicator of tumor hypoxia and its expression was clearly down-regulated in dissected tumors treated with MnO_2-contained AuNRs (Figure 5d). Meanwhile, a series of studies demonstrated that TAMs were likely polarized into M2 TAMs in the hypoxia tumor microenvironment, while normoxia-benefited M1 TAMs polarization for cancer therapy.[19,20,24,37,38] We therefore studied the polarization of macrophages in dissect tumors by immunochemical analysis in Figure 5e. CD206 and CD80 are the hallmarks of M2 and M1 macrophages, respectively. It is clearly observed that CD206 was highly-expressed in control group. After the treatment of AuNRs containing MnO_2, the expression of CD206 was down-regulated while CD80 expression was enhanced (Figure 5e). This was a direct evidence for M1 polarization by hypoxia relief. We also detected the pro-inflammatory cytokine IL-12 and anti-inflammatory IL-10 in Figure S9a,b, Supporting Information. IL-12 expression was higher in laser groups than without laser groups. This was consistent with better anti-tumor ability of the laser-irradiated groups. IL-10 expression had no obvious discrepancy in AuNRs treated groups even under the laser irradiation. This could be due to the M1 polarization of macrophages. Taking together, these results demonstrated that combining PTT-induced ICD and MnO_2-mediated hypoxia relief boosted anti-tumor immunotherapy. This system not only enhanced the tumor-derived antigen release but also improved the tumor microenvironment.

We further investigated biocompatibility of the AuNRs. As shown in Figure S10, Supporting Information, the AuNRs did not have any significant influence either on mice's weight (Figure S10a, Supporting Information) or on the damage to major tissue of mice (Figure S10c, Supporting Information). Considering the components of AuNR@BSA/MnO_2, its dual-imaging function was studied, which could be employed for therapeutic guidance and even for evaluation of tumoral accumulation. From MRI in Figure S11a, Supporting Information, it not only traced the tumor area but also verified that AuNR@BSA/MnO_2 could penetrate into tumor area by EPR (enhanced penetration and retention). PAI was also performed by recording the deoxygenated hemoglobin (Hb, 780 nm) and oxygenated hemoglobin (HbO_2, 850 nm) after 12 h i.v.[39] Both AuNR@BSA/MnO_2 and AuNR@BSA showed obvious PAI signals (Figure S11b, Supporting Information), while AuNR@BSA/MnO_2 showed a higher intensity in 850 nm than AuNR@BSA, which could be regarded as another evidence for hypoxia relief. The MRI and PAI functions of AuNR@BSA/MnO_2 will expand its application in future study.

2.6. Combination with Anti-PD-1 Checkpoint Therapy

Encouraged by the AuNRs-mediated ICD and macrophage polarization, we hypothesized that such AuNRs would have a synergistic effect with the PD-1 checkpoint blockade therapy. Therefore, we explored the distant effect by combination with the PD-1 checkpoint blockade therapy. A bilateral tumor model was constructed as **Figure 6**a. When tumors reached 50 mm^3, mice were divided into different groups, and the left tumors were treated by AuNRs with laser irradiation. 20 mg kg^{-1} PD-1 inhibitor was adopted on day 3, 5, and 7 by intraperitoneal injection. As expected, the primary tumors were almost ablated and the distant tumors were also delayed when the anti-PD-1 therapy was applied in Figure 6b,c. Apart from the distant effect for secondary tumor, we also explored whether this synergistic effect would benefit the survival. A survival model was constructed as Figure 6d. Mice with tumor inoculation were treated with the AuNRs and laser irradiation on day 0 and 20 mg kg^{-1} PD-1 inhibitor was adopted on day 3, 5, and 7 by intraperitoneal injection. The survival of the mice was monitored and exhibited in Figure 6e. In the group of AuNR@BSA/MnO_2 with laser irradiation and PD-1 checkpoint blockade therapy, all tumors were ablated and shown no death as long as 60 days. It was clear that the AuNRs combining with the checkpoint blockade therapy not only demonstrated effective distant effect but also benefited the survival.

Apart from the bilateral tumor model, we also constructed a metastatic model to support the distant effect by synergistic

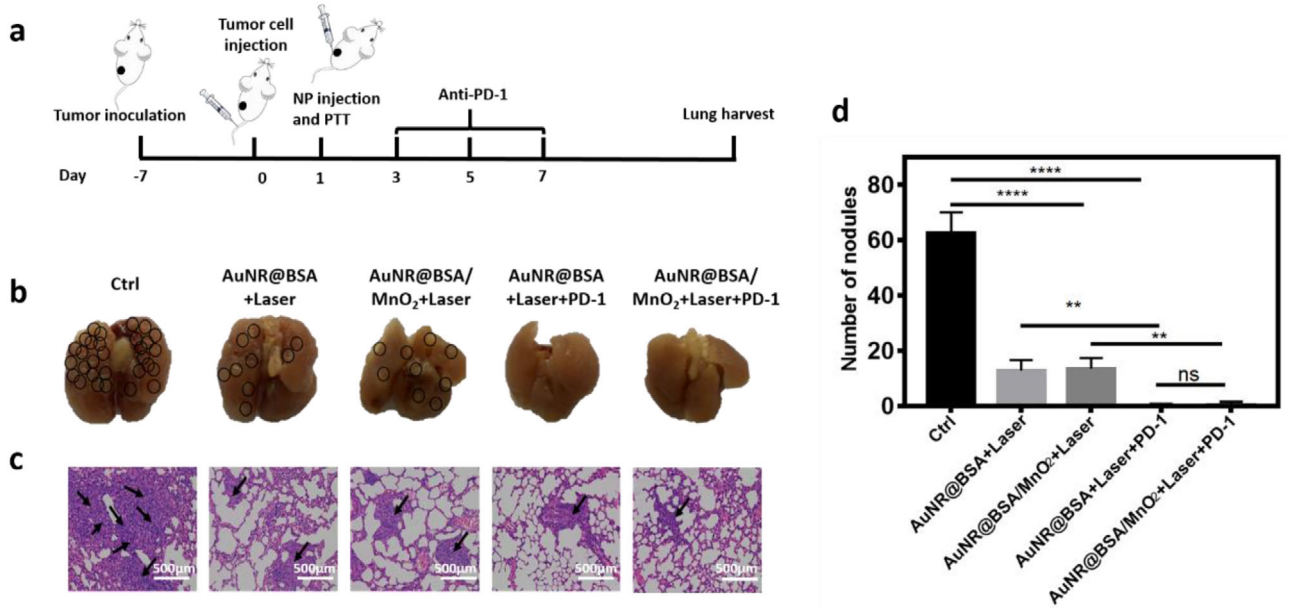

Figure 7. Anti-metastasis by synergistic effect with checkpoint blockade therapy. a) Scheme of anti-metastasis model. b) Representative photos of metastatic nodules on lung surface under different treatments. c) Hematoxylin–eosin staining of lung in indicated groups. Black arrows represented the metastatic nodules. d) Numbers of metastatic nodules of lung in indicated groups. Data was shown by mean ± SD, $^{****}p < 0.0001$.

therapy as **Figure 7**a. Tumor-bearing mice were first treated with the AuNRs and laser irradiation. Then, tumor cells were injected intravenously to simulate the metastatic nodules. After that, 20 mg kg^{-1} PD-1 inhibitor was injected on day 3, 5, and 7. As shown in Figure 7b–d, metastatic nodules in the lung sharply decreased under the AuNR@BSA + Laser and AuNR@BSA/MnO_2 + Laser therapies. More excitingly, there were almost no nodules left when the two therapies were combined with the checkpoint blockade therapy. This excellent anti-metastatic efficacy was attributed to the synergistic effect and also another demonstration of distant effect.

3. Conclusion

In summary, we designed a multifunctional AuNR@BSA/MnO_2 to address the current limitations of anti-tumor immunotherapy. AuNR@BSA/MnO_2 was designed and constructed by combing the PTT property of AuNR and the oxygenating activity of MnO_2. By combining the PTT-induced ICD and hypoxia improvement-benefited M1 polarization simultaneously, the AuNR@BSA/MnO_2 exhibited good anti-tumor efficacy. Additionally, by synergizing with a checkpoint blockade therapy, notable distant effect was demonstrated including anti-secondary tumor, anti-metastasis, and even prolonging the survival. Furthermore, the AuNR@BSA/MnO_2 had dual imaging functions like MRI and PAI. Considering the clinical success of immunotherapy and the great achievements in nanotherapeutics, the design strategy demonstrated in the current study will advance new combined anti-tumor therapies by taking the advantages of both and may eventually benefit cancer patients in the future.

4. Experimental Section

Chemicals and Materials: Hydrogen tetrachloroaurate (III) tetrahydrate ($HAuCl_4{\cdot}4H_2O$), silver nitrate ($AgNO_3$), sodium borohydride ($NaBH_4$), ascorbic acid (AA), and bovine serum albumin (BSA) were purchased from Sigma-Aldrich (Shanghai, China). Hydrogen peroxide (H_2O_2), hydrochloric acid (HCl), and sodium hydroxide (NaOH) were obtained from Shanghai Sinopharm Chemical Reagent Co., Ltd. (Shanghai, China). Reagents for cell culture, including fetal bovine serum (FBS), phosphate buffer (PBS), high glucose DMEM, penicillin, and streptomycin, were from Thermo Fisher (Thermo Fisher Scientific, China). ATP detection kit and detection antibodies were from Beyotime Biotechnology Co., Ltd. (Shanghai, China). 4T1 cell line (murine mammary cancer cell) was supplied by ATCC. CCK-8 kit was purchased from DONJINDO (Kumamoto, Japan). Nuclear dye Hochest 33342 was from Sangon Biotech (Shanghai, China). Hypoxia detection kit was from Enzo Life Science Inc. (NY, USA). Mouse IFN γ ELISA kit and TNF α Elisa kit were from Neobioscience Technology Co, Ltd. (Shanghai, China). All reagents were used as received without further purification. Deionized water was used in all experiments (18.2 MΩ·cm, Millipore).

Instrumentation: UV–visible–NIR absorption spectra were detected by a spectrophotometer (UV-3600 plus, Shimadzu, Japan). Scanning electron microscopy (SEM) images were obtained by a Zeiss Ultra 55 scanning electron microscope operating at 3 kV. Transmission electron microscopy (TEM) images were got by a JEOL JEM-2100 transmission electron microscope with an acceleration voltage of 200 kV. Absorption values of microplates were collected by SpectraMax M2/M2e (Molecular Devices, US). Dynamic lighting scattering and zeta-potential distribution were measured by a Nanosizer ZS90 (Malvern Zetasizer, Malvern). Magnetic resonance imaging was performed on a 7.0 T small animal MR Scanner (Bruker PharmaScan, Germany). IR thermographic camera ThermaCAM SC3000 of FLIR (Boston, USA) was used for thermal-imaging and AnalyzIR software for data analysis. Dissolved oxygen was monitored by a SevenExcellence Multiparameter of METTLER TOLEDO Co., Ltd. (Zürich, Swiss).

Synthesis of AuNRs: AuNRs were synthesized by a seed-mediated method according to the previous studies. [23,27] Briefly, the Au seed solution was prepared as follows. $HAuCl_4$ (2 mg mL^{-1}, 0.5 mL) and CTAB

(0.2 M, 4.75 mL) mixed together, then fresh $NaBH_4$ (0.017 mM, 1 mL) was injected fleetly. The reaction solution was stirred vigorously for 2 min. Then the Au seed solution was kept under room condition. The Au growth solution was prepared by first mixing $HAuCl_4$ (2 mg mL^{-1}, 10 mL) with NaOl (sodium oleate) and CTAB solution (NaOl: 0.064 g, CTAB: 0.325 g in 15 mL of water). After completely mixing, $AgNO_3$ (4 mM, 0.2 mL) and ascorbic acid (0.064 M, 120 µL) were injected into the $HAuCl_4$/NaOl/CTAB solution to get the growth solution. To grow AuNRs, 80 µL of Au seeding solution was added into the growth solution and then kept at 28 °C for 12 h under mild stirring. AuNRs were harvested after centrifugation.

Preparation of AuNR@BSA and AuNR@BSA/MnO_2: AuNR@BSA was prepared as per the reported studies.[28] 2.5 mL 0.5 mM BSA was added into 50 mL of AuNRs solution, and incubated for 12 h with mild stirring at room temperature. The excess BSA was removed by centrifugation.

AuNR@BSA/MnO_2 was prepared by adding $KMnO_4$ (5 mg mL^{-1}, 1 mL) into AuNR@BSA solution (50 mL) and stirring for 12 h. Then AuNR@BSA/MnO_2 was harvested by centrifugation.

Cell Culture and Cytotoxicity Analysis: 4T1 and RAW 264.7 cells were cultured with 10% FBS and high glucose DMEM at 37 °C in a 5% CO_2 incubator. For cell viability analysis, cells were subcultured into 96-well plates at 8×10^3 cells per well overnight, then cells were treated with NPs with appropriate concentrations. After the treatments, Cell Counting Kit-8 (CCK-8) assay was used to assess the cell viability. For PTT experiments in vitro, cells were treated with an 808 nm laser for 5 min at 1 W cm^{-2} after different AuNRs treated 12 h.

Ability of Decomposition H_2O_2 into O_2: MnO_2 would endow the oxygenating ability of AuNR@BSA/MnO_2. 5 mM H_2O_2 and 20 µg mL^{-1} AuNR@BSA/MnO_2 were incubated together in PBS; the oxygen production was measured by a dissolved oxygen 335 meter (SevenExcellence Multiparameter, Mettler Toledo Co., Ltd.).

ATP Detection: ATP detection was performed according to the protocol of the ATP detection kit. Briefly, cells were incubated with different NPs (10 µg mL^{-1}) for 12 h, then were irradiated by an 808 nm laser for 5 min at 1 W cm^{-2}. The cell culture medium and cells were collected at 4 and 12 h after laser irradiation, respectively. Supernatant solution of cells' lysate and cultured medium were used for luminescence ATP detection, which was based on the ATP-mediated luciferin luminescence. Each experiment was carried out independently four times.

Immunofluorescence of HMGB1 and CRT In Vitro: The cells were treated with NPs for 12 h, and were irradiated for 5 min at 1 W cm^{-2} 808 nm laser, then were cultured for another 12 h. The cells were washed with PBS for three times and fixed with 4% paraformaldehyde for 4 min. Later the cells were washed, blocked, and incubated with antibody (HMGB1 rabbit monoclonal antibody and CRT rabbit monoclonal antibody, respectively) for 2 h. After that, the cells were washed with PBS and incubated with FITC-labeled goat anti-rabbit IgG (H + L) for 1 h. Last, the cells were washed and stained with Hochest 33342. Imaging was executed by CLSM. FITC: EX/EM 488 nm/520 nm, Hochest 33342: EX/EM 350 nm/460 nm.

Hypoxia Relief In Vitro: Oxygen generation ability of MnO_2 was monitored by a Hypoxia Detection Kit in vitro. Cells were subcultured into dishes, the cells were treated with different AuNRs for 4 h then substituted culture medium containing hypoxia detection reagent and hypoxia inducer deferoxamine (DFO, 200 µM final concentration) for 3.5 h. Cells were gently washed, fixed, and stained with Hochest 33342, then CLSM (confocal laser scanning microscopy, IX-83 Olympus & Andor) was executed to observe the fluorescence. Hypoxia probe: EX/EM 570 nm/596 nm, Hochest 33342: EX/EM 350 nm/460 nm.

Anti-Tumor Model In Vivo: All the animal studies were approved by the Committee for Experimental Animals Welfare and Ethics of Nanjing Drum Tower Hospital, the Affiliated Hospital of Nanjing University Medical School. For anti-tumor model, Babl/c mice (male, 4–6 weeks, ≈20 g) were purchased from Nanjing Medical University and raised in specific pathogen free (SPF) environment. 4T1 cells were harvested, suspended into PBS then subcutaneously injected into right upper extremity area with the 1×10^6 cells per mouse. When the volume of tumor reached 100 mm^3 (volume calculated according to the formula $V = \text{length} \times \text{width} \times \text{width}/2$, the length and width were measured by digital calipers), mice were separated into five groups with randomization, and treated with designed NPs (5 mg kg^{-1}) by intravenous injection and given laser irradiation (808 nm for 5 min at 2 W cm^{-2}).

Immunofluorescence of HMGB1 and CRT In Vivo: The mice were sacrificed and the tumors were dissected. Then tumors were mounted with OCT compound. 5 µm slices were separated by microtone, the slices were blocking–washing–incubating–staining according to standard procedures. Last imaging was carried out by CLSM. The percent of the released HMGB1 was calculated by measuring the fluorescent intensity using Image J and setting no treated cells as the blank.

Quantification of Cytokines in Serum of Peripheral Blood: After AuNRs injection and laser irradiation, peripheral blood was collected at 12 h for IL10, IL12, TNF α, and IFN γ detection. Blood was left at room temperature for 20 min to clot, then centrifuged to obtain serum. The levels of IL10, IL12, TNF α and IFN γ were detected by Enzyme-Linked Immunosorbent Assay (ELISA) kits respectively, operated according to standard manuals. Each experiment was carried out independently four times.

Photothermal Effect In Vivo: To evaluate the photothermal effect, tumor-bearing mice were irradiated with an 808 nm laser at the tumor area for 5 min at 2 W cm^{-2}. Photothermal imaging was performed by IR camera with certain time interval, then the detail temperature was analyzed by AnalyzIR software.

Histopathology Evaluation: When mice were sacrificed, the major organs including heart, liver, spleen, lung, and kidney were collected for hematoxylin and eosin (H&E) staining. Imaging was carried out by microscope, and representative images were captured.

MRI and PAI Imaging: To investigate the multifunction of AuNRs, MRI and PAI imaging were executed. Mice were treated with different AuNRs (5 mg kg^{-1}) by intravenous injection. After 24 h, MRI imaging was performed on a 7.0 T small animal MR Scanner (Bruker PharmaScan, Germany). PAI imaging was carried out by a photoacoustic computed tomography scanner after 12 h i.v., and images were reconstructed by OsiriX MD software.

Supporting Information

Supporting Information is available from the Wiley Online Library or from the author.

Acknowledgements

The authors thank Chao Zhang, Bin Li, Yihong Zhang, and Quan Wang for help with experiments. This work was supported by National Natural Science Foundation of China (91859112, 21722503, and 21874067), the China Postdoctoral Science Foundation (2019TQ0144 and 2019M661786), PAPD program, Open Funds of the State Key Laboratory of Coordination Chemistry (SKLCC1819), and Fundamental Research Funds for the Central Universities (021314380145 and 021414380485).

Conflict of Interest

The authors declare no conflict of interest.

Keywords

cancer immunotherapy, gold nanorods, hypoxic tumor microenvironment, immunogenic cell death, photothermal therapy

Received: August 24, 2020
Revised: October 15, 2020
Published online: November 13, 2020

[1] D. M. Pardoll, *Nat. Rev. Cancer* **2012**, *12*, 252.
[2] Q. Chen, Q. Hu, E. Dukhovlinova, G. Chen, S. Ahn, C. Wang, E. A. Ogunnaike, F. S. Ligler, G. Dotti, Z. Gu, *Adv. Mater.* **2019**, *31*, 1900192.
[3] P. Gotwals, S. Cameron, D. Cipolletta, V. Cremasco, A. Crystal, B. Hewes, B. Mueller, S. Quaratino, C. Sabatos-Peyton, L. Petruzzelli, J. A. Engelman, G. Dranoff, *Nat. Rev. Cancer* **2017**, *17*, 286.
[4] J. B. A. G. Haanen, *Cell* **2017**, *170*, 1055.
[5] P. Sharma, S. Hu-Lieskovan, J. A. Wargo, A. Ribas, *Cell* **2017**, *168*, 707.
[6] A. Ribas, J. D. Wolchok, *Science* **2018**, *359*, 1350.
[7] T. F. Gajewski, H. Schreiber, Y.-X. Fu, *Nat. Immunol.* **2013**, *14*, 1014.
[8] D. K.-C. Chiu, A. P.-W. Tse, I. M.-J. Xu, J. Di Cui, R. K.-H. Lai, L. L. Li, H.-Y. Koh, F. H.-C. Tsang, L. L. Wei, C.-M. Wong, I. O.-L. Ng, C. C.-L. Wong, *Nat. Commun.* **2017**, *8*, 517.
[9] Y. Ma, S. Adjemian, S. R. Mattarollo, T. Yamazaki, L. Aymeric, H. Yang, J. P. P. Catani, D. Hannani, H. Duret, K. Steegh, I. Martins, F. Schlemmer, M. Michaud, O. Kepp, A. Q. Sukkurwala, L. Menger, E. Vacchelli, N. Droin, L. Galluzzi, R. Krzysiek, S. Gordon, P. R. Taylor, P. Van Endert, E. Solary, M. J. Smyth, L. Zitvogel, G. Kroemer, *Immunity* **2013**, *38*, 729.
[10] C. Yue, P. Liu, M. Zheng, P. Zhao, Y. Wang, Y. Ma, L. Cai, *Biomaterials* **2013**, *34*, 6853.
[11] F. Zhou, S. Wu, S. Song, W. R. Chen, D. E. Resasco, D. Xing, *Biomaterials* **2012**, *33*, 3235.
[12] Z. Wang, P. Huang, O. Jacobson, Z. Wang, Y. Liu, L. Lin, J. Lin, N. Lu, H. Zhang, R. Tian, G. Niu, G. Liu, X. Chen, *ACS Nano* **2016**, *10*, 3453.
[13] S. J. Martin, C. M. Henry, S. P. Cullen, *Mol. Cell* **2012**, *46*, 387.
[14] H. Inoue, K. Tani, *Cell Death Differ.* **2014**, *21*, 39.
[15] J. R. Melamed, R. S. Edelstein, E. S. Day, *ACS Nano* **2015**, *9*, 6.
[16] Y. Ma, Y. Zhang, X. Li, Y. Zhao, M. Li, W. Jiang, X. Tang, J. Dou, L. Lu, F. Wang, Y. Wang, *ACS Nano* **2019**, *13*, 11967.
[17] J. Nam, S. Son, L. J. Ochyl, R. Kuai, A. Schwendeman, J. J. Moon, *Nat. Commun.* **2018**, *9*, 1074.
[18] L. Li, S. Yang, L. Song, Y. Zeng, T. He, N. Wang, C. Yu, T. Yin, L. Liu, X. Wei, Q. Wu, Y. Wei, L. Yang, C, Gong, *Theranostics* **2018**, *8*, 860.
[19] G. Yang, L. Xu, Y. Chao, J. Xu, X. Sun, Y. Wu, R. Peng, Z. Liu, *Nat. Commun.* **2017**, *8*, 902.
[20] M. Song, T. Liu, C. Shi, X. Zhang, X. Chen, *ACS Nano* **2016**, *10*, 633.
[21] M. Zhou, X. Wang, S. Lin, Y. Cheng, S. Zhao, J. Lin, Z. Fang, Z. Lou, L. Qin, H. Wei, *Adv. Healthcare Mater.* **2020**, *9*, 2000064.
[22] T. Lin, X. Zhao, S. Zhao, H. Yu, W. Cao, W. Chen, H. Wei, H. Guo, *Theranostics* **2018**, *8*, 990.
[23] X. Ye, L. Jin, H. Caglayan, J. Chen, G. Xing, C. Zheng, V. Doan-Nguyen, Y. Kang, N. Engheta, C. R. Kagan, C. B. Murray, *ACS Nano* **2012**, *6*, 2804.
[24] P. Prasad, C. R. Gordijo, A. Z. Abbasi, A. Maeda, A. Ip, A. M. Rauth, R. S. DaCosta, X. Y. Wu, *ACS Nano* **2014**, *8*, 3202.
[25] T. Lin, X. Zhao, S. Zhao, H. Yu, W. Cao, W. Chen, H. Wei, H. Guo, *Theranostics* **2018**, *8*, 990.
[26] C. Ding, Y. Xu, Y. Zhao, H. Zhong, X. Luo, *ACS Appl. Mater. Interfaces* **2018**, *10*, 8947.
[27] B. Nikoobakht, M. A. El-Sayed, *Chem. Mater.* **2003**, *15*, 1957.
[28] M. R. K. Ali, S. R. Panikkanvalappil, M. A. El-Sayed, *J. Am. Chem. Soc.* **2014**, *136*, 4464.
[29] Q. Chen, L. Feng, J. Liu, W. Zhu, Z. Dong, Y. Wu, Z. Liu, *Adv. Mater.* **2016**, *28*, 7129.
[30] G. Kroemer, L. Galluzzi, O. Kepp, L. Zitvogel, *Annu. Rev. Immunol.* **2013**, *31*, 51.
[31] D. V. Krysko, A. D. Garg, A. Kaczmarek, O. Krysko, P. Agostinis, P. Vandenabeele, *Nat. Rev. Cancer* **2012**, *12*, 860.
[32] M. T. Lotze, K. J. Tracey, *Nat. Rev. Immunol.* **2005**, *5*, 331.
[33] I. Martins, Y. Wang, M. Michaud, Y. Ma, A. Q. Sukkurwala, S. Shen, O. Kepp, D. Métivier, L. Galluzzi, J. L. Perfettini, L. Zitvogel, G. Kroemer, *Cell Death Differ.* **2014**, *21*, 79.
[34] M. Obeid, A. Tesniere, F. Ghiringhelli, G. M. Fimia, L. Apetoh, J.-L. Perfettini, M. Castedo, G. Mignot, T. Panaretakis, N. Casares, D. Métivier, N. Larochette, P. van Endert, F. Ciccosanti, M. Piacentini, L. Zitvogel, G. Kroemer, *Nat. Med.* **2007**, *13*, 54.
[35] S. Basu, P. K. Srivastava, *J. Exp. Med.* **1999**, *189*, 797.
[36] M. Z. Noman, M. Hasmim, A. Lequeux, M. Xiao, C. Duhem, S. Chouaib, G. Berchem, B. Janji, *Cells* **2019**, *8*, 1083.
[37] Y. He, C. Cong, Z. Liu, X. Li, R. Zhu, D. Gao, *Chem. Eng. J.* **2019**, *378*, 122252.
[38] Y. He, C. Cong, Y. He, Z. Hao, C. Li, S. Wang, Q. Zhao, H. He, R. Zhu, X. Li, D. Gao, *Chem. Eng. J.* **2019**, *375*, 122079.
[39] G. Diot, S. Metz, A. Noske, E. Liapis, B. Schroeder, S. V. Ovsepian, R. Meier, E. Rummeny, V. Ntziachristos, *Clin. Cancer. Res.* **2017**, *23*, 6912.